BIOPHYSICS

Directional mechanical stability of Bacteriophage ϕ29 motor's 3WJ-pRNA: Extraordinary robustness along portal axis

Zhonghe Xu,[1,2]* Yang Sun,[3]* Jeffrey K. Weber,[4] Yi Cao,[3] Wei Wang,[3] Daniel Jasinski,[5] Peixuan Guo,[5] Ruhong Zhou,[1,4,6†] Jingyuan Li[1,2†]

2017 © The Authors, some rights reserved; exclusive licensee American Association for the Advancement of Science. Distributed under a Creative Commons Attribution NonCommercial License 4.0 (CC BY-NC).

The molecular motor exploited by bacteriophage ϕ29 to pack DNA into its capsid is regarded as one of the most powerful mechanical devices present in viral, bacterial, and eukaryotic systems alike. Acting as a linker element, a prohead RNA (pRNA) effectively joins the connector and ATPase (adenosine triphosphatase) components of the ϕ29 motor. During DNA packing, this pRNA needs to withstand enormous strain along the capsid's portal axis—how this remarkable stability is achieved remains to be elucidated. We investigate the mechanical properties of the ϕ29 motor's three-way junction (3WJ)–pRNA using a combined steered molecular dynamics and atomic force spectroscopy approach. The 3WJ exhibits strong resistance to stretching along its coaxial helices, demonstrating its super structural robustness. This resistance disappears, however, when external forces are applied to the transverse directions. From a molecular standpoint, we demonstrate that this direction-dependent stability can be attributed to two Mg clamps that cooperate and generate mechanical resistance in the pRNA's coaxial direction. Our results suggest that the asymmetric nature of the 3WJ's mechanical stability is entwined with its biological function: Enhanced rigidity along the portal axis is likely essential to withstand the strain caused by DNA condensation, and flexibility in other directions should aid in the assembly of the pRNA and its association with other motor components.

INTRODUCTION

Bacillus subtilis bacteriophage ϕ29 uses an ATP (adenosine 5′-triphosphate)–driven molecular motor to pack its viral DNA into its crowning capsid (*1*). This packing motor can overcome the considerable energies associated with strand bending and interstrand repulsion in its DNA substrates; capable of generating ~20 pN of force, the ϕ29 motor is, thus, regarded as one of the strongest molecular motors ever characterized (*2*, *3*). Composed of a dodecameric head-tail connector embedded in the capsid, an oligomeric prohead RNA (pRNA) ring, and an adenosine triphosphatase (ATPase) gp16 ring, the ϕ29 motor drives double-stranded DNA into exceptionally high packing densities while maintaining its structure under the large forces induced by DNA confinement (*3*–*8*). The operation of this motor has been demonstrated to depend on Mg^{2+} ions, perhaps suggesting a critical structural role for the pRNA that joins the connector and ATPase domains (*9*, *10*).

The core structure of the pRNA domain is composed of three major helices organized into a three-way junction (3WJ)-pRNA (Fig. 1A) (*6*, *11*, *12*). Helix 1 (H1) of the 3WJ-pRNA connects to the pRNA's ATPase-binding region (motif 1); helices 2 and 3 (H2/3) are attached to the pRNA's right-handed and left-handed loops (motifs 2 and 3), respectively, which are involved in pRNA oligomerization and binding with the motor's connector domain (*6*, *8*, *13*–*15*). Together, this 3WJ-pRNA links the connector- and ATPase-binding regions of the motor's full pRNA domain. In relation to the structure of the ϕ29 motor, H1 and H3 are stacked coaxially and parallel to the motor's portal axis (*7*, *12*). During the DNA packing process, the pressure induced by DNA confinement can reach beyond 50 atm along this coordinate (*3*, *16*). As the linker between the connector and ATPase domains, the 3WJ-pRNA thus bears a considerable portion of the mechanical force exerted along the portal axis (*6*, *13*–*15*, *17*). The mechanical stability of the 3WJ-pRNA should therefore be critical for maintaining the structural integrity of the ϕ29 motor as it operates.

The mechanical stabilities of nucleic acid structures—including DNA double helices and RNA hairpins, G-quadruplexes, and pseudoknots—are generally low, featuring rupture forces of a few tens of piconewtons (*18*–*26*). Unlike within mechanically stable proteins, such as titin and ubiquitin, poor coupling of hydrogen bonds within nucleic structures usually limits their tolerance of applied forces. A natural question thus arises: How can the 3WJ-pRNA within the ϕ29 motor resist the considerable external forces brought about by DNA confinement? Recently, 3WJ-pRNAs have been exploited to construct RNA nanoparticles by fusing aptamer-, small interfering RNA (siRNA)–, or receptor-binding ligands to various arms of the 3WJ motif (*27*–*32*). Encouragingly, the global structure of 3WJ-pRNAs is largely retained in the resulting nanoparticles, suggesting that the 3WJ structure does exhibit mechanical and thermodynamic stability in isolation.

Here, we evaluate the mechanical stability of the ϕ29 motor's 3WJ-pRNA using steered molecular dynamics (SMD) simulations and atomic force microscopy (AFM). We find that this 3WJ-pRNA exhibits exceptional mechanical stability, withstanding forces up to 220 ± 78 pN along the H1-H3 portal axis (forces higher than many canonically stable proteins can tolerate). This extraordinary mechanical resistance can largely be attributed to the coordination of two Mg^{2+} ions to the 3WJ motif, which sustain the native RNA structure by anchoring two of its strands in cooperative fashion. We further investigate the 3WJ-pRNA's in situ functional dynamics by emulating its interactions with the neighboring pRNA

[1]Institute of Quantitative Biology and Department of Physics, Zhejiang University, Hangzhou, Zhejiang 310027, China. [2]Key Laboratory for Biomedical Effects of Nanomaterials and Nanosafety, Institute of High Energy Physics, Chinese Academy of Sciences, Beijing 100049, China. [3]Collaborative Innovation Center of Advanced Microstructures, National Laboratory of Solid State Microstructure, Department of Physics, Nanjing University, Nanjing, Jiangsu 210093, China. [4]IBM Thomas J. Watson Research Center, Yorktown Heights, NY 10598, USA. [5]Center for RNA Nanobiotechnology and Nanomedicine, College of Pharmacy, Division of Pharmaceutics and Pharmaceutical Chemistry; College of Medicine/Department of Physiology & Cell Biology; Dorothy M. Davis Heart and Lung Research Institute, The Ohio State University, Columbus, OH 43210, USA. [6]Department of Chemistry, Columbia University, New York, NY 10027, USA.
*These authors contributed equally to this work.
†Corresponding author. Email: lijingyuan@ihep.ac.cn (J.L.); ruhongz@us.ibm.com (R.Z.)

Downloaded from http://advances.sciencemag.org/ on January 18, 2018

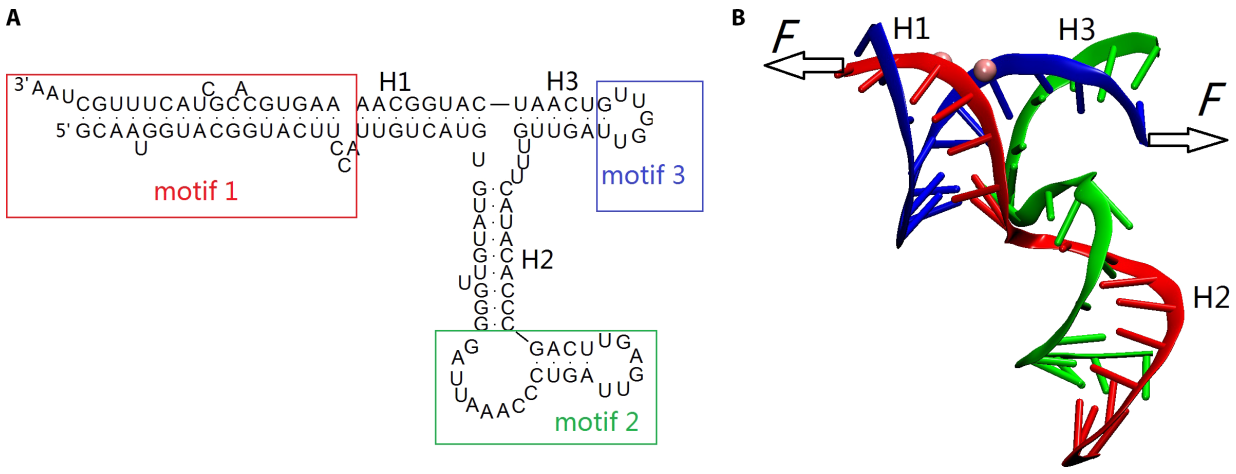

Fig. 1. Schematic illustration of the 3WJ-pRNA and related SMD simulations. (**A**) The ϕ29 motor's full-length pRNA, containing a core 3WJ structure and exterior motifs 1, 2, and 3. (**B**) The scheme used for loading force onto the helix termini. RNA strands A, B, and C are colored in red, green, and blue, respectively, in this and subsequent figures.

and connector domains. Under these conditions, the 3WJ-pRNA still resists coaxial mechanical forces (intended to mimic forces along the portal axis that occur during DNA packaging) quite well. The remarkable stability of the ϕ29 motor's 3WJ-pRNA is believed to be crucial for its biological function, as we discuss below.

RESULTS AND DISCUSSION

As noted previously, the core region of the ϕ29 motor's pRNA domain is composed of three RNA strands (designated here as strands A, B, and C) that comprise three helices (H1, H2, and H3) in the folded 3WJ. Two Mg^{2+} ions bind in the major groove between H1 and H3 (Fig. 1B). Experiments indicate that H1 and H3 are largely stacked coaxially and parallel to the portal axis, making them bear the brunt of forces generated by the motor (*7*, *12*). Hence, we first studied the mechanical properties of the 3WJ-pRNA along its H1-H3 axis. Sixteen independent simulations were performed by pulling the helix termini at a rate of 0.1 nm/ns (fig. S1).

The 3WJ-pRNA shows exceptional resistance to the applied force, exhibiting a large average rupture force of 1990 ± 126 pN and maintaining its native structure before unfolding (Fig. 2). As shown in a representative trajectory, the root mean square deviation (RMSD) of the 3WJ-pRNA remains around 3.5 Å until the appearance of the dominant force peak (~40 ns; Fig. 2A); the number of hydrogen bonds within the 3WJ-pRNA also remains constant over the same time interval (fig. S2A). Similar phenomena can be seen in unfolding simulations at pulling rates of 0.01 and 1 nm/ns, for which average rupture forces of 1854 ± 72 and 2217 ± 77 pN were observed (figs. S3 and S4). Because the coaxial H1 and H3 are parallel to the motor's portal axis, the observed mechanical stability ensures that the pRNA can resist the strain along the capsid's portal, likely helping to maintain the structure of the motor during DNA packing.

As the pulling proceeds, another force peak appears around $t = 85$ ns because of the relative reconfiguration of strand C with respect to strands A and B (fig. S2B). The resistance associated with this sliding process is also considerable, yielding a rupture force of ~500 pN. Hence, 3WJ-pRNA unfolding appears to occur over two stages: An initial dramatic unfolding event is followed by rearrangements among the RNA strands. This three-state unfolding mechanism seems to endow the 3WJ-pRNA with extraordinary mechanical resilience. The existence of a stable intermediate state perhaps allows the pRNA domain to regain its original structure after the initial unfolding event, a safeguard that would help preserve the 3WJ's biological function.

The extraordinary mechanical stability observed during the first stage of pulling arises from the coordination of Mg^{2+} ions with H1 and H3 (Fig. 3). As revealed by RNA crystal structure, two pairs of phosphates [G23 (H1) and A90 (H3); C24 (H1) and A89 (H3)] act to bind two Mg^{2+} ions, forming two Mg clamps parallel to the shared axis of H1 and H3 and adjacent to one another (*12*). These clamps resist external forces along the helical axis in a cooperative fashion, maintaining the structure of the 3WJ-pRNA during pulling. The interphosphate distances between G23 and A90 and between C24 and A89 illustrate the persistence and cooperativity of these Mg structures (Fig. 3B): Both interphosphate separations remain steadfast near 4 Å before the first dramatic unfolding event near 2000 pN, at which point the Mg clamps simultaneously break and H1 and H3 unfold. This concerted rupture of Mg clamps and subsequent loss of RNA structure can also be seen in unfolding processes with other pulling rates (fig. S5).

To more clearly demonstrate the importance of bound Mg^{2+} ions for the 3WJ's stability, we removed both Mg^{2+} ions from the initial configuration and performed SMD simulations on the Mg-free RNA (Fig. 2A). As hypothesized, the mechanical resistance associated with the first stage of pulling totally disappears in the absence of Mg coordination. Instead, both the H1 and H3 quickly unfold under the applied force, as one might expect with standard nucleic acid helices (*18*–*23*). The second force peak, corresponding to strand reconfiguration after Mg clamp rupture, is retained in the Mg-free system. The role of Mg^{2+} ions in maintaining the mechanical stability of the 3WJ-pRNA was verified using an alternative magnesium model (fig. S6). In further control simulations, Mg^{2+} ions were replaced by Ca^{2+} ions and resistance to stretching disappeared (see discussion S1 and figs. S7 and S8).

We also assessed the stability of the Mg^{2+}-bound 3WJ in transverse directions, loading force onto the termini of H1-H2 and H2-H3 (figs. S9 and S10). In both cases, only a small force peak appears corresponding to strand register shifts that occur after the RNA has mostly unfolded. These results suggest that the 3WJ only resists large forces applied along its H1-H3 axis. Simple physical arguments justify our observations of rapid unfolding under transverse pulling conditions. First, under transverse forces, H2 and its perpendicular counterparts are coerced to rotate

Downloaded from http://advances.sciencemag.org/ on January 18, 2018

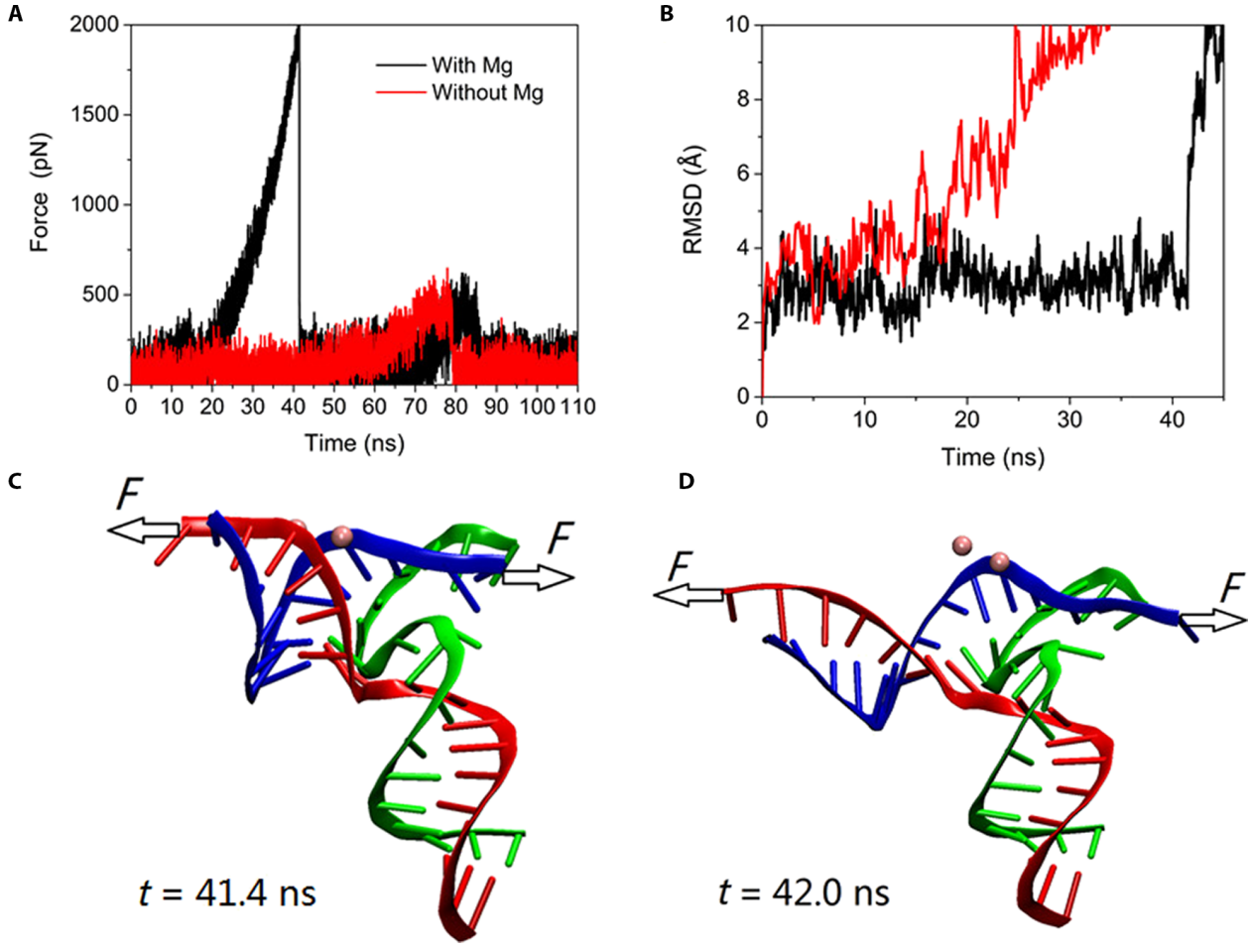

Fig. 2. Mechanical unfolding of 3WJ-pRNA under coaxial pulling conditions. (**A**) Force profile of the 3WJ-pRNA with and without bound Mg^{2+} ions. (**B**) The RMSD of the 3WJ-pRNA structures with (black) and without (red) bound Mg^{2+} ions under applied pulling forces. (**C** and **D**) Representative snapshots of the 3WJ-pRNA at t = 41.4 and 42.0 ns (that is, before and after the initial unfolding event near t = 41.5 ns).

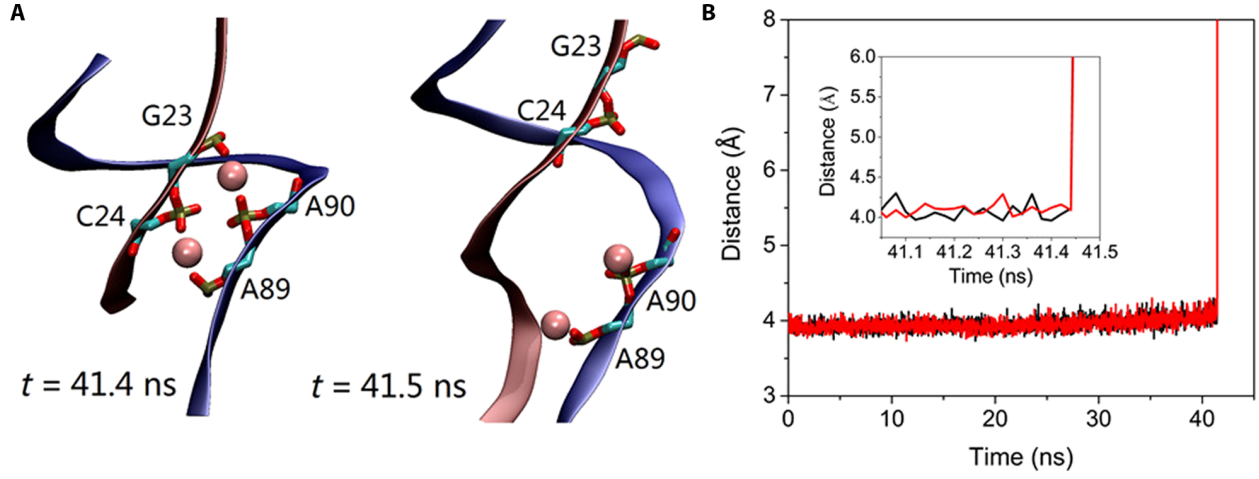

Fig. 3. Rupture of Mg clamps during mechanical unfolding. (**A**) Coordination interactions of Mg^{2+} ions during unfolding. (**B**) Interphosphate separation between nucleotides G23 and A90 (black) and C24 and A89 (red) over the course of pulling. Inset: Zoom-in of the interphosphate separation near the rupture of the two Mg clamps.

Downloaded from http://advances.sciencemag.org/ on January 18, 2018

and align with the pulling coordinate, resulting in considerable distortion of the 3WJ's structure. Second, H2 does not contribute nucleotides to the 3WJ's Mg clamps, suggesting that its helical structure should be particularly vulnerable to mechanical disruption.

We thus find that the mechanical stability of the ϕ29 motor's 3WJ-pRNA is highly sensitive to the particular pulling coordinate. This asymmetry in the 3WJ's stability is perhaps important for its function: Although stout rigidity along the H1-H3 axis is likely crucial for resisting the enormous strain applied on the motor during DNA packing, flexibility in other directions should facilitate the interdomain binding needed for prohead assembly (*17*).

To explore the 3WJ's mechanical resistance under more biomimetic conditions, we also simulated a configuration of the pRNA that emulates connections to other motor components (that is, the connector, the ATPase, and the adjacent pRNA; Fig. 4 and fig. S11). As revealed by past experiments, H2 and H3 connect to the pRNA's chiral loops and, ultimately, the motor's connector domain (motifs 2 and 3; Fig. 1A); H1 is attached to the pRNA's ATPase-binding region (motif 1; Fig. 1A) (*6*, *13*–*15*). Accordingly, to reproduce the effects of the connector domain and adjacent pRNA loops, we restrained both ends of H2 and H3 to their initial positions. The impact of the portal axis strain that occurs during motor operation was then simulated by applying force along the H1-H3 coordinate from the H1 terminus (Fig. 4, A and B). Across 16 independent simulation runs, we again found that the 3WJ exhibits extraordinary mechanical stability in the coaxial direction (Fig. 4C), featuring an average rupture force of 2020 ± 144 pN. The cooperative Mg clamps once more play a crucial role in mediating force resistance: The dramatic pRNA's extension that occurs near t = 38 ns closely corresponds to the simultaneous rupture of the two Mg clamps, as indicated by the interphosphate distances (Fig. 4C, inset). This striking mechanical stability once more disappears in the absence of Mg^{2+} ions (Fig. 4C). These results indicate that the 3WJ-pRNA can perhaps even better resist the strain associated with DNA packing when placed in biomimetic configurations.

One can also estimate the lifetime of the 3WJ-pRNA's folded state under an applied constant force (here, held at both 1600 and 2000 pN across 120 independent simulations). As shown in figs. S12 and S13 and Fig. 4D, the unfolding of the 3WJ-pRNA in the presence of Mg clamps can be well described as a single-exponential, two-state process. A first-order kinetic model suggests that the survival probability of the folded state should decay as a simple exponential: $P(t) = \exp[-k(F)t]$. The unfolding rates derived from fits to this model are $k = 0.025 \pm 2.6 \times 10^{-4}$ ns^{-1} (F = 1600 pN) and k = 4.94 ± 0.39 ns^{-1} (F = 2000 pN), respectively.

Under the two-state reaction regime, the relationship between the unfolding rate and the loading force is described by $k(F) = k_0 \exp(F\Delta x/k_B T)$,

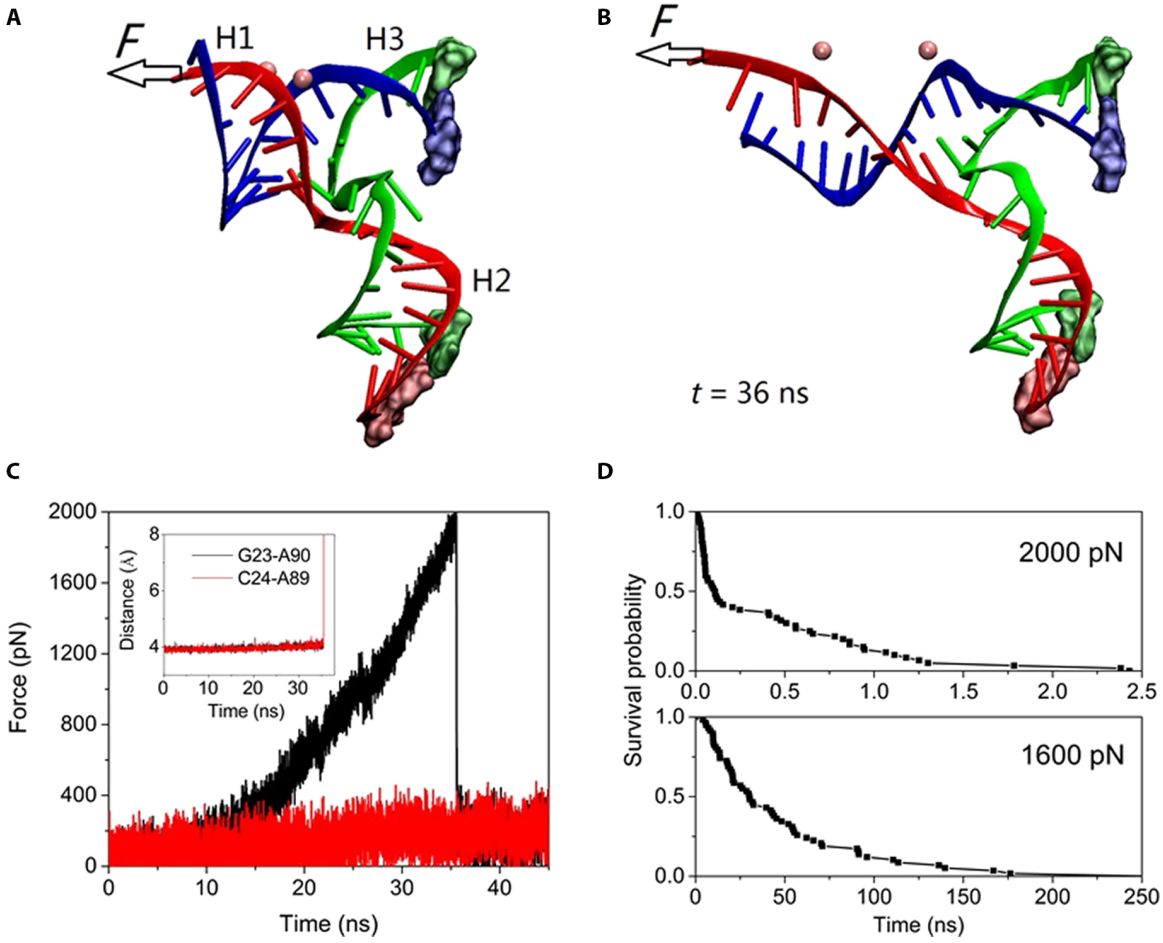

Fig. 4. Mechanical unfolding of the 3WJ-pRNA under biomimetic conditions. (**A**) Schematic for the loading force onto the H1 terminus of the 3WJ-pRNA. Restrained nucleotides are shown in a van der Waals representation. (**B**) Representative configuration of the 3WJ-pRNA after initial unfolding. (**C**) Force profile of the 3WJ-pRNA with (black) and without (red) bound Mg^{2+} ions. Inset: Interphosphate distances associated with the two Mg clamps. (**D**) Survival curves for the unfolding of the 3WJ-pRNA under loading forces of 1600 and 2000 pN.

Downloaded from http://advances.sciencemag.org/ on January 18, 2018

where k_0 is the unfolding rate at zero force and Δx is the distance to transition state (*33*). After combining this equation with the two unfolding rates drawn from simulations, we estimate $k_0 = 0.0078\ s^{-1}$ and $\Delta x = 0.56$ Å, and the extrapolated unfolding rate is only about $0.0103\ s^{-1}$ when $F = 20$ pN (the force exerted by the ϕ29 ATPase). We thus estimate the lifetime of folded state under operational load, reciprocal to the reaction rate, to be approximately 97 s. This long lifetime suggests that the ϕ29 motor's 3WJ-pRNA can easily resist the strain encountered over the course of DNA packing. Similarly, the relationship between the rupture force and the loading rate measured in constant-velocity SMD simulations at different pulling rates was used to estimate values for k_0 and Δx on the basis of the Bell-Evans equation. The folded state lifetime at $F = 20$ pN was extrapolated to be 64 s (see discussion S2 and fig. S14).

To corroborate these simulation results, we also performed single-molecule force spectroscopy experiments on the ϕ29 motor's 3WJ-pRNA. The termini of H1 and H3 were first attached with polyethylene glycol (PEG) linkers to the AFM cantilever tip and substrate, respectively (Fig. 5A); the rupture force of 3WJ-pRNA was then measured by stretching the RNA's termini at pulling rate of 1000 nm/s. Note that, by necessity, SMD simulations were conducted using an extremely high pulling rate from an experimental perspective (1×10^8 nm/s). As a result, experimentally measured rupture forces should be considerably smaller than those estimated from simulations. Extrapolations of folded state lifetimes at constant force, however, can be used for making direct comparisons between simulation and experiment.

The two force-extension curves shown in Fig. 5B are representative of 3WJ-pRNA unfolding in the presence of Mg^{2+} ions. The extension observed before rupture is presumably due to the reversal of entropic elasticity effects, which draw the polymer termini together at equilibrium. Applying a worm-like chain model (red line; Fig. 5B) to each force-extension curve measurement, binning the results, and fitting the histogram to a Gaussian function yield an average rupture force estimate of 220 ± 78 pN (Fig. 5C). This measured stability is higher than that of many so-called mechanical proteins, such as GB1 and fibronectin, and is comparable to that of the strongest mechanical protein (the titin I27 domain) (*34*–*38*). Treating the system with EDTA to remove coordinated Mg^{2+} ions, the average rupture force is markedly reduced to 70 ± 22 pN (Fig. 5D). In a manner consistent with our simulation results, therefore, these experiments demonstrate that the ϕ29 motor's 3WJ-pRNA exhibits high, Mg^{2+}-dependent mechanical stability along its H1-H3 axis.

We also measured the rupture force for the 3WJ-pRNA at various loading rates, ranging from 1×10^4 to 1.5×10^5 pN/s (Fig. 5E). The rupture force increases with logarithm of loading rate, r, as described by the Bell-Evans equation: $F(r) = (k_B T/\Delta x) \ln[r\Delta x/(k_0 k_B T)]$ (Fig. 5E) (*39*). The unfolding rate at a loading force of 20 pN (the force exerted by the ϕ29 ATPase), k_{20}, is thus estimated as $0.039\ s^{-1}$ (see discussion S2). Accordingly, the lifetime of folded state, τ_{20}, is approximately 26 s, a value on the same order of magnitude as that estimated from SMD simulations. These estimates of τ_{20} are much longer than the lifetimes of many other RNA structures (such as hairpins, riboswitch, and pseudoknots) (*20*–*23*, *25*, *26*), suggesting this Mg-bound 3WJ motif plays a unique role in maintaining the structure of the ϕ29 motor.

CONCLUSIONS

Here, we have probed the mechanical properties of the ϕ29 molecular motor's 3WJ-pRNA using SMD simulations and atomic force spectroscopy. We find that the 3WJ-pRNA exhibits remarkable mechanical stability along its portal axis, resisting forces even higher than what can be withstood by a variety of mechanically stable proteins (*34*–*38*). This extraordinary mechanical stability can largely be attributed to two Mg clamps located in the major groove between helices 1 and 3 of the 3WJ, which act to resist coaxial strain in cooperative fashion.

As revealed by past experiments, Mg^{2+} ions assist in the assembly of the ϕ29 motor's pRNA domain. Our findings suggest that Mg^{2+} ions are also essential for the 3WJ-pRNA to maintain its structure during the motor's operation. This mechanical stability does not extend in

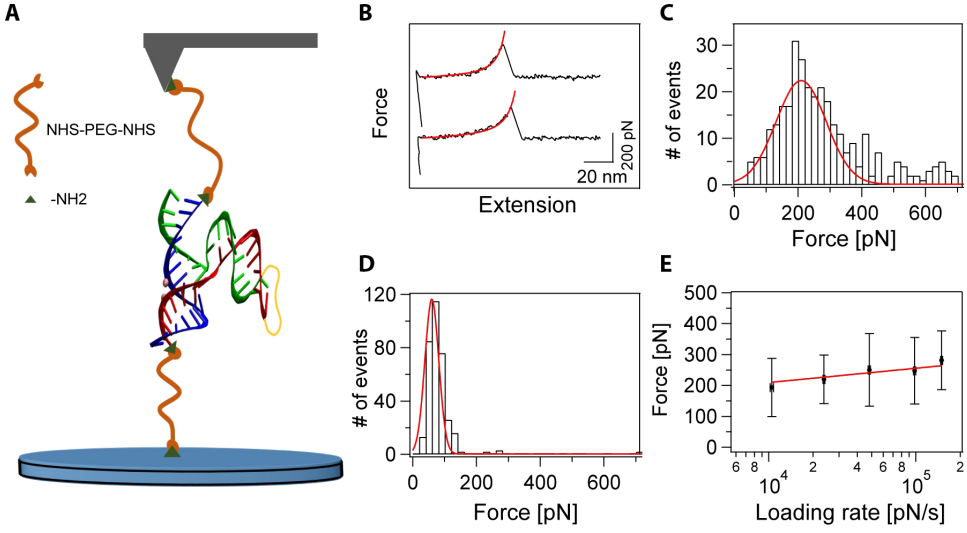

Fig. 5. AFM experiments of 3WJ-pRNA's unfolding along H1-H3. (**A**) Schematic for AFM-based single-molecule force spectroscopy experiments. Both the cantilever tip and the glass substrate were modified with amine groups using APTES. Bifunctional PEG linkers were used to covalently link the 5′ amine–modified H1 to the substrate and H3 to the cantilever tip. (**B**) Two typical force-extension curves for the rupture of the 3WJ-pRNA in TMS buffer [89 mM tris, 5mM $MgCl_2$ (pH 7.6)]. (**C**) Rupture force histogram for traces shown in (B). (**D**) Rupture force histogram for the unfolding in tris buffer [89 mM tris, 20 mM EDTA (pH 7.6)]. (**E**) Dependence of the rupture force on the loading rate for the unfolding in TMS buffer.

Downloaded from http://advances.sciencemag.org/ on January 18, 2018

transverse directions (along the H1-H2 and H2-H3 axes that are not stabilized by Mg clamps). As noted above, this asymmetry in the 3WJ-pRNA's mechanical properties could be important for the ϕ29 motor's function. Rigidity along the portal axis is required so that the motor's pRNA domain can withstand the strain caused by DNA condensation, whereas flexibility in transverse directions should facilitate assembly of the pRNA and its binding to the capsid prohead (*17*). The duplicity in structural persistence perhaps sheds light on the evolutionary design process that gave rise to this remarkable molecular motor.

Note that pRNAs in other bacteriophage motors adopt similar structures to the 3WJ-pRNA studied here and that Mg^{2+} ions are also known to be crucial for these motors' functions. Thus, we speculate that Mg^{2+} ions play a similar important role in stabilizing these molecular motors, which forms the structural basis for rigid structures (somewhat like connecting rods) that are essential for optimal motor performance. Furthermore, our findings about the potential for cooperation among Mg clamps to endow RNAs with exceptional mechanical resistance could serve to explain the existence of and guide the design of an array of robust nucleic acid structures.

MATERIALS AND METHODS

SMD simulations

As noted above, the core structure of the pRNA studied here consists of three major helices (H1, H2, and H3) organized as a 3WJ (*29*). The structure of this 3WJ-pRNA was obtained from the protein data bank (code 4KZ2) (*12*). In this crystal structure, two divalent metal ion–binding sites were identified inside the major groove between H1 and H3 (*12*). Although Mn^{2+} ions were used to discover these putative metal-binding sites in experiments, physiologically relevant Mg^{2+} ions were found to occupy the same coordination sites as these Mn^{2+} ions (*12*). Hence, configurations of the 3WJ-pRNA bound with (and, as a control, free of) Mg^{2+} ions were constructed for use in simulations. Three base pairs attached to the terminus of H3 (fig. S15) were also omitted from the structural analysis. The prepared 3WJ-pRNA configurations were solvated with the TIP3P water model, and Na^+ and Cl^- ions were added to neutralize the system and bring its total ionic strength to 100 mM (*40*). Each 3WJ-pRNA structure was independently relaxed using a 50-ns equilibration simulation (P = 1 atm, T = 300 K).

SMD simulations were next used to study the mechanical properties of the 3WJ-pRNA. Within the structure of the connector-pRNA complex in the ϕ29 motor, H1 and H3 of the 3WJ-pRNA are coaxial and oriented along the portal axis. Hence, we first studied a situation in which external forces were applied to the termini of H1 and H3. The rupture force, measured in constant-velocity SMD simulations, was used to estimate the mechanical stabilities of 3WJ-pRNA in isolation. A series of constant-velocity SMD simulations were performed with progressive pulling velocities of 0.01, 0.1, and 1 nm/ns and loading rates of 16.61, 166.1, 1661 pN/ns across 8, 16, and 16 independent simulation runs, respectively. To emulate a configuration in which the pRNA is contained within the ϕ29 motor (and subject to the constraints of the full pRNA and connector domains), we conducted similar SMD runs in which the H2 and H3 termini were fixed; in these cases, both constant force (with 1600 and 2000 pN loading forces) and constant velocity (166.1 pN/ns loading rate) SMD simulations were performed. To establish the stabilizing role of Mg^{2+} ions, we also performed constant-velocity SMD simulations with a loading rate of 166.1 pN/ns in the absence of bound magnesium. To probe the impact of transverse mechanical strain on the 3WJ's stability, we further loaded forces onto the termini of H1 and H2 and H2 and H3 in independent constant-velocity runs. All SMD simulations were carried out within the constant volume and temperature (NVT) ensemble at a temperature of 300 K.

The dimensions of the simulation box were adjusted according to different pulling parameters (see table S1 for more information). All simulations were conducted using the GROMACS 5.1 simulation package and the AMBER14 force field (*41*–*44*). The Mg^{2+} ion model developed by Allner *et al.* was used in all primary simulation runs (*45*). To validate our simulation results, another Mg^{2+} ion model and two Ca^{2+} ion models were also studied (see table S2 and discussion S1 for more information) (*46*, *47*). Periodic boundary conditions were applied in all directions. Short-range electrostatic and van der Waals interactions were calculated at a cutoff distance of 12 Å, whereas long-range electrostatic interactions were treated using the particle mesh Ewald method (*48*). The Nose-Hoover thermostat and the Parrinello-Rahman barostat were chosen for temperature and pressure control, respectively (*49*–*51*). Simulation snapshots were rendered in visual molecular dynamics (*52*).

AFM-based single-molecule force spectroscopy

5′-Modified RNA strands (strands A + B and C, in the above nomenclature) were purchased from GenScript. Bifunctionalized PEG linkers [*N*-hydroxyl succinimide (NHS)–PEG–NHS; (5000 Da) conjugated to the terminal amine-reacting group NHS, were purchased from Jenkem. All other chemicals were purchased from Sigma-Aldrich and used without further purification.

Glass coverslides were placed in hot chromium acid (80°C) for 0.5 hours to remove residual organic matter and generate hydroxyl groups on their surfaces. These coverslides were then rinsed with Milli-Q water and dried under a nitrogen stream. Subsequently, each dried coverslide was dipped in a toluene solution containing 0.1% (v/v) of 3-aminopropyl triethoxysilane (APTES) for 1 hour and afterward rinsed with toluene, dried under a nitrogen stream, and further incubated in a drying oven at 80°C for 20 min. The coverslides were then dipped in a DMSO (dimethyl sulfoxide) solution containing NHS-PEG-NHS (0.1 mg/ml) at room temperature for ~90 min, rinsed with sterile distilled water, and placed in a solution containing RNA strands A + B (~30 ng/μl) at 4°C for 90 min. Finally, each sample was incubated in tris buffer (50 mM, pH 6) for 30 min to block free NHS groups. Cantilevers (MLCT, type D, Bruker) were modified using the same protocol applied to the glass coverslide substrates, except that the RNA strand C was used.

Single-molecule AFM experiments were performed on a commercial AFM (NanoWizard II, JPK Instruments). In the force spectroscopy experiments, modified cantilevers and substrates were placed directly in either 1× TMS [89 mM tris, 5 mM $MgCl_2$ (pH 7.6)] or tris buffer [89 mM tris, 20 mM EDTA (pH 7.6)]. Note that this 3WJ-pRNA is known to exhibit considerable chemical stability, resisting denaturation in at least 4 M urea (*29*). On the basis of the equipartition theorem, cantilevers with a spring constant of ~40 pN/nm were then calibrated after equilibrating for ~30 min. The force spectroscopy curves were recorded using JPK software and then analyzed by a home-written protocol in Igor 6.37 (WaveMetrics). Pulling speeds were converted to loading rates following a preestablished procedure (*53*). First, force-extension curves were converted to force-time curves. The average slopes of the force-time curves right before the rupture event were then computed to estimate the average loading rate for the nonequilibrium, constant-velocity pulling process. In this way, the contribution of the stiffness of the whole mechanical linkage—including the cantilever, the PEG linker, and the ligand receptor—to the loading rate was taken into account. The rupture force histograms were fitted with standard Gaussian distribution.

Downloaded from http://advances.sciencemag.org/ on January 18, 2018

SUPPLEMENTARY MATERIALS

Supplementary material for this article is available at http://advances.sciencemag.org/cgi/content/full/3/5/e1601684/DC1

discussion S1. Divalent ion models studied in this work and the corresponding results.
discussion S2. Extrapolation of lifetime of folded state to the loaded force of 20 pN from SMD simulations and AFM experiments
table S1. The dimension of simulation systems.
table S2. The parameters of divalent ions.
fig. S1. Force profiles during the unfolding along H1-H3 (16 trajectories).
fig. S2. Structural analysis of 3WJ-pRNA during the unfolding along H1-H3.
fig. S3. Force profiles of 3WJ-pRNA during the unfolding along H1-H3 (eight trajectories).
fig. S4. Force profiles during the unfolding along H1-H3 (pulling rate is 1 nm/ns).
fig. S5. Cooperativity of two Mg clamps during mechanical unfolding.
fig. S6. Force profiles during the unfolding along H1-H3 using the Merz model of Mg^{2+} ions.
fig. S7. Relaxation and mechanical unfolding of 3WJ-pRNA using the Aqvist model of Ca^{2+} ions.
fig. S8. Relaxation and mechanical unfolding of 3WJ-pRNA using the Merz model of Ca^{2+} ions.
fig. S9. Mechanical unfolding of 3WJ-pRNA under transverse (H1-H2) pulling.
fig. S10. Mechanical unfolding of 3WJ-pRNA under transverse (H2-H3) pulling.
fig. S11. Force profiles of 3WJ-pRNA with force applied to the termini of H1 at a pulling rate of 0.1 nm/ns.
fig S12. Representative length-time traces of 3WJ-pRNA when constant force is loaded onto the terminus of H1.
fig S13. Distribution of unfolding times for the pRNA-3WJ under the loading forces of 1600 and 2000 pN.
fig. S14. Dependence of the rupture force on the loading rate.
fig. S15. Schematic of 3WJ-pRNA in the crystal structure (4KZ2), where three base pairs (bold) are attached to the terminus of H3.
References (*54*–*56*)

REFERENCES AND NOTES

1. P. X. Guo, T. J. Lee, Viral nanomotors for packaging of dsDNA and dsRNA. *Mol. Microbiol.* **64**, 886–903 (2007).
2. J. P. Rickgauer, D. N. Fuller, S. Grimes, P. J. Jardine, D. L. Anderson, D. E. Smith, Portal motor velocity and internal force resisting viral DNA packaging in bacteriophage ϕ29. *Biophys. J.* **94**, 159–167 (2008).
3. D. E. Smith, S. J. Tans, S. B. Smith, S. Grimes, D. L. Anderson, C. Bustamante, The bacteriophage straight ϕ29 portal motor can package DNA against a large internal force. *Nature.* **413**, 748–752 (2001).
4. P. Guo, S. Bailey, J. W. Bodley, D. Anderson, Characterization of the small RNA of the bacteriophage φ29 DNA packaging machine. *Nucleic Acids Res.* **15**, 7081–7090 (1987).
5. P. X. Guo, S. Erickson, D. Anderson, A small viral RNA is required for in vitro packaging of bacteriophage phi 29 DNA. *Science* **236**, 690–694 (1987).
6. P. Guo, C. Zhang, C. Chen, K. Garver, M. Trottier, Inter-RNA interaction of phage ϕ29 pRNA to form a hexameric complex for viral DNA transportation. *Mol. Cell* **2**, 149–155 (1998).
7. A. A. Simpson, Y. Tao, P. G. Leiman, M. O. Badasso, Y. He, P. J. Jardine, N. H. Olson, M. C. Morais, S. Grimes, D. L. Anderson, T. S. Baker, M. G. Rossmann, Structure of the bacteriophage ϕ29 DNA packaging motor. *Nature* **408**, 745–750 (2000).
8. T.-J. Lee, P. Guo, Interaction of gp16 with pRNA and DNA for genome packaging by the motor of bacterial virus phi29. *J. Mol. Biol.* **356**, 589–599 (2006).
9. C. Chen, P. Guo, Magnesium-induced conformational change of packaging RNA for procapsid recognition and binding during phage ϕ29 DNA encapsidation. *J. Virol.* **71**, 495–500 (1997).
10. Y. Hao, J. S. Kieft, Diverse self-association properties within a family of phage packaging RNAs. *RNA* **20**, 1759–1774 (2014).
11. X. Zhang, C.-S. Tsung, G. Z. Sowa, M. M. Hatmal, I. S. Haworth, P. Z. Qin, Global structure of a three-way junction in a phi29 packaging RNA dimer determined using site-directed spin labeling. *J. Am. Chem. Soc.* **134**, 2644–2652 (2012).
12. H. Zhang, J. A. Endrizzi, Y. Shu, F. Haque, C. Sauter, L. S. Shlyakhtenko, Y. Lyubchenko, P. Guo, Y.-l. Chi, Crystal structure of 3WJ core revealing divalent ion-promoted thermostability and assembly of the Phi29 hexameric motor pRNA. *RNA* **19**, 1226–1237 (2013).
13. C. Zhang, C.-S. Lee, P. Guo, The proximate 5′ and 3′ ends of the 120-base viral RNA (pRNA) are crucial for the packaging of bacteriophage ϕ29 DNA. *Virology* **201**, 77–85 (1994).
14. F. Zhang, S. Lemieux, X. Wu, D. St.-Arnaud, C. T. McMurray, F. Major, D. Anderson, Function of hexameric RNA in packaging of bacteriophage ϕ29 DNA in vitro. *Mol. Cell* **2**, 141–147 (1998).
15. K. Garver, P. Guo, Boundary of pRNA functional domains and minimum pRNA sequence requirement for specific connector binding and DNA packaging of phage ϕ29. *RNA* **3**, 1068–1079 (1997).
16. M. Hernando-Pérez, R. Miranda, M. Aznar, J. L. Carrascosa, I. A. T. Schaap, D. Reguera, P. J. de Pablo, Direct measurement of phage phi29 stiffness provides evidence of internal pressure. *Small* **8**, 2366–2370 (2012).
17. W. Zhao, M. Saha, A. Ke, M. C. Morais, P. J. Jardine, S. Grimes, A three-helix junction is the interface between two functional domains of prohead RNA in ϕ29 DNA packaging. *J. Virol.* **86**, 11625–11632 (2012).
18. S. B. Smith, Y. Cui, C. Bustamante, Overstretching B-DNA: The elastic response of individual double-stranded and single-stranded DNA molecules. *Science* **271**, 795–799 (1996).
19. M. Rief, H. Clausen-Schaumann, H. E. Gaub, Sequence-dependent mechanics of single DNA molecules. *Nat. Struct. Biol.* **6**, 346–349 (1999).
20. J. Liphardt, B. Onoa, S. B. Smith, I. Tinoco Jr., C. Bustamante, Reversible unfolding of single RNA molecules by mechanical force. *Science* **292**, 733–737 (2001).
21. L. Green, C.-H. Kim, C. Bustamante, I. Tinoco Jr., Characterization of the mechanical unfolding of RNA pseudoknots. *J. Mol. Biol.* **375**, 511–528 (2008).
22. G. Chen, K.-Y. Chang, M.-Y. Chou, C. Bustamante, I. Tinoco Jr., Triplex structures in an RNA pseudoknot enhance mechanical stability and increase efficiency of −1 ribosomal frameshifting. *Proc. Natl. Acad. Sci. U.S.A.* **106**, 12706–12711 (2009).
23. D. B. Ritchie, D. A. N. Foster, M. T. Woodside, Programmed -1 frameshifting efficiency correlates with RNA pseudoknot conformational plasticity, not resistance to mechanical unfolding. *Proc. Natl. Acad. Sci. U.S.A.* **109**, 16167–16172 (2012).
24. P. M. Yangyuoru, A. Y. Q. Zhang, Z. Shi, D. Koirala, S. Balasubramanian, H. Mao, Mechanochemical properties of individual human telomeric RNA (TERRA) G-quadruplexes. *Chembiochem* **14**, 1931–1935 (2013).
25. W. J. Greenleaf, K. L. Frieda, D. A. N. Foster, M. T. Woodside, S. M. Block, Direct observation of hierarchical folding in single riboswitch aptamers. *Science* **319**, 630–633 (2008).
26. Z. Yu, V. Gaerig, Y. Cui, H. Kang, V. Gokhale, Y. Zhao, L. H. Hurley, H. Mao, Tertiary DNA structure in the single-stranded hTERT promoter fragment unfolds and refolds by parallel pathways via cooperative or sequential events. *J. Am. Chem. Soc.* **134**, 5157–5164 (2012).
27. S. Guo, F. Huang, P. Guo, Construction of folate-conjugated pRNA of bacteriophage phi29 DNA packaging motor for delivery of chimeric siRNA to nasopharyngeal carcinoma cells. *Gene Ther.* **13**, 814–820 (2006).
28. F. Xiao, Y. Cai, J. C.-Y. Wang, D. Green, R. H. Cheng, B. Demeler, P. Guo, Adjustable ellipsoid nanoparticles assembled from re-engineered connectors of the bacteriophage phi29 DNA packaging motor. *ACS Nano* **3**, 2163–2170 (2009).
29. D. Shu, Y. Shu, F. Haque, S. Abdelmawla, P. Guo, Thermodynamically stable RNA three-way junction for constructing multifunctional nanoparticles for delivery of therapeutics. *Nat. Nanotechnol.* **6**, 658–667 (2011).
30. Y. Shu, M. Cinier, S. R. Fox, N. Ben-Johnathan, P. Guo, Assembly of therapeutic pRNA-siRNA nanoparticles using bipartite approach. *Mol. Ther.* **19**, 1304–1311 (2011).
31. F. Haque, D. Shu, Y. Shu, L. S. Shlyakhtenko, P. G. Rychahou, B. M. Evers, Peixuan Guo, Ultrastable synergistic tetravalent RNA nanoparticles for targeting to cancers. *Nano Today* **7**, 245–257 (2012).
32. D. Shu, H. Li, Y. Shu, G. Xiong, W. E. Carson, F. Haque, R. Xu, P. Guo, Systemic delivery of anti-miRNA for suppression of triple negative breast cancer utilizing RNA nanotechnology. *ACS Nano* **9**, 9731–9740 (2015).
33. G. I. Bell, Models for the specific adhesion of cells to cells. *Science* **200**, 618–627 (1978).
34. M. Carrion-Vazquez, A. F. Oberhauser, S. B. Fowler, P. E. Marszalek, S. E. Broedel, J. Clarke, J. M. Fernandez, Mechanical and chemical unfolding of a single protein: A comparison. *Proc. Natl. Acad. Sci. U.S.A.* **96**, 3694–3699 (1999).
35. P. E. Marszalek, H. Lu, H. Li, M. Carrion-Vazquez, A. F. Oberhauser, K. Schulten, J. M. Fernandez, Mechanical unfolding intermediates in titin modules. *Nature* **402**, 100–103 (1999).
36. R. B. Best, S. B. Fowler, J. L. T. Herrera, A. Steward, E. Paci, J. Clarke, Mechanical unfolding of a titin Ig domain: Structure of transition state revealed by combining atomic force microscopy, protein engineering and molecular dynamics simulations. *J. Mol. Biol.* **330**, 867–877 (2003).
37. M. Carrion-Vazquez, H. Li, H. Lu, P. E. Marszalek, A. F. Oberhauser, J. M. Fernandez, The mechanical stability of ubiquitin is linkage dependent. *Nat. Struct. Biol.* **10**, 738–743 (2003).
38. Y. Cao, T. Yoo, H. Li, Single molecule force spectroscopy reveals engineered metal chelation is a general approach to enhance mechanical stability of proteins. *Proc. Natl. Acad. Sci. U.S.A.* **105**, 11152–11157 (2008).
39. E. Evans, K. Ritchie, Dynamic strength of molecular adhesion bonds. *Biophys. J.* **72**, 1541–1555 (1997).

Downloaded from http://advances.sciencemag.org/ on January 18, 2018

40. W. L. Jorgensen, J. Chandrasekhar, J. D. Madura, R. W. Impey, M. L. Klein, Comparison of simple potential functions for simulating liquid water. *J. Chem. Phys.* **79**, 926–935 (1983).
41. A. Perez, I. Marchán, D. Svozil, J. Sponer, T. E. Cheatham III, C. A. Laughton, M. Orozco, Refinement of the AMBER force field for nucleic acids: Improving the description of α/γ conformers. *Biophys. J.* **92**, 3817–3829 (2007).
42. B. Hess, C. Kutzner, D. van der Spoel, E. Lindahl, GROMACS 4: Algorithms for highly efficient, load-balanced, and scalable molecular simulation. *J. Chem. Theory Comput.* **4**, 435–447 (2008).
43. M. Zgarbova, M. Otyepka, J. Šponer, A. Mládek, P. Banáš, T. E. Cheatham, P. Jurečka, Refinement of the Cornell et al. nucleic acids force field based on reference quantum chemical calculations of glycosidic torsion profiles. *J. Chem. Theory Comput.* **7**, 2886–2902 (2011).
44. I. S. Joung, T. E. Cheatham III, Determination of alkali and halide monovalent ion parameters for use in explicitly solvated biomolecular simulations. *J. Phys. Chem. B* **112**, 9020–9041 (2008).
45. O. Allner, L. Nilsson, A. Villa, Magnesium ion–water coordination and exchange in biomolecular simulations. *J. Chem. Theory Comput.* **8**, 1493–1502 (2012).
46. J. Aqvist, Ion-water interaction potentials derived from free energy perturbation simulations. *J. Phys. Chem.* **94**, 8021–8024 (1990).
47. P. Li, B. P. Roberts, D. K. Chakravorty, K. M. Merz Jr., Rational design of particle mesh Ewald compatible Lennard-Jones parameters for +2 metal cations in explicit solvent. *J. Chem. Theory Comput.* **9**, 2733–2748 (2013).
48. T. Darden, D. York, L. Pedersen, Particle mesh Ewald: An *N*-log(*N*) method for Ewald sums in large systems. *J. Chem. Phys.* **98**, 10089–10092 (1993).
49. M. Parrinello, A. Rahman, Polymorphic transitions in single crystals: A new molecular dynamics method. *J. Appl. Phys.* **52**, 7182–7190 (1981).
50. W. G. Hoover, Canonical dynamics: Equilibrium phase-space distributions. *Phys. Rev. A* **31**, 1695–1697 (1985).
51. K. M. Aoki, F. Yonezawa, Constant-pressure molecular-dynamics simulations of the crystal-smectic transition in systems of soft parallel spherocylinders. *Phys. Rev. A* **46**, 6541–6549 (1992).
52. W. Humphrey, A. Dalke, K. Schulten, VMD: Visual molecular dynamics. *J. Mol. Graph. Model.* **14**, 33–38 (1996).
53. T. Strunz, K. Oroszlan, R. Schäfer, H.-J. Güntherodt, Dynamic force spectroscopy of single DNA molecules. *Proc. Natl. Acad. Sci. U.S.A.* **96**, 11277–11282 (1999).
54. O. K. Dudko, J. Mathé, A. Szabo, A. Meller, G. Hummer, Extracting kinetics from single-molecule force spectroscopy: Nanopore unzipping of DNA hairpins. *Biophys. J.* **92**, 4188–4195 (2007).
55. O. K. Dudko, G. Hummer, A. Szabo, Theory, analysis, and interpretation of single-molecule force spectroscopy experiments. *Proc. Natl. Acad. Sci. U.S.A.* **105**, 15755–15760 (2008).
56. A. A. Chen, A. E. García, Mechanism of enhanced mechanical stability of a minimal RNA kissing complex elucidated by nonequilibrium molecular dynamics simulations. *Proc. Natl. Acad. Sci. U.S.A.* **109**, E1530–E1539 (2012).

Acknowledgments: J.L. acknowledges the Special Program for Applied Research on Super Computation of the National Natural Science Foundation of China (NSFC)–Guangdong Joint Fund (the second phase). **Funding:** This work is partially supported by the National Basic Research Program of China (973 Program) grants 2013CB933704 and 2013CB834100 and NSFC grants 21473207, 11374221, 21273240, 21522402, 11334004, and 11574224 and NIH EB019036 for funding. R.Z. acknowledges the support of the IBM Blue Gene Science Program (W1258591, W1464125, W1464164). **Author contributions:** J.L. and R.Z. designed the study. Z.X. and J.L. performed molecular dynamics (MD) simulations and analysis, Y.S. and Y.C. performed the AFM experiments. All authors discussed the results and contributed to the writing of the manuscript. **Competing interests:** P.G.'s Sylvan G. Frank Endowed Chair position in Pharmaceutics and Drug Delivery is funded by the CM Chen Foundation. P.G. is a consultant for Oxford Nanopore Technologies and Nanobio Delivery Pharmaceutical Co. Ltd. and a cofounder of Shenzhen P&Z BioMedical Co. Ltd and its subsidiary U.S. P&Z Biological Technology LLC. All other authors declare that they have no competing interests. **Data and materials availability:** All data needed to evaluate the conclusions in the paper are present in the paper and/or the Supplementary Materials. Additional data related to this paper may be requested from the authors.

Submitted 20 July 2016
Accepted 7 April 2017
Published 26 May 2017
10.1126/sciadv.1601684

Citation: Z. Xu, Y. Sun, J. K. Weber, Y. Cao, W. Wang, D. Jasinski, P. Guo, R. Zhou, J. Li, Directional mechanical stability of Bacteriophage ϕ29 motor's 3WJ-pRNA: Extraordinary robustness along portal axis. *Sci. Adv.* **3**, e1601684 (2017).

Downloaded from http://advances.sciencemag.org/ on January 18, 2018

Science Advances

Directional mechanical stability of Bacteriophage ϕ29 motor's 3WJ-pRNA: Extraordinary robustness along portal axis

Zhonghe Xu, Yang Sun, Jeffrey K. Weber, Yi Cao, Wei Wang, Daniel Jasinski, Peixuan Guo, Ruhong Zhou and Jingyuan Li

Sci Adv **3** (5), e1601684.
DOI: 10.1126/sciadv.1601684

ARTICLE TOOLS http://advances.sciencemag.org/content/3/5/e1601684

SUPPLEMENTARY MATERIALS http://advances.sciencemag.org/content/suppl/2017/05/22/3.5.e1601684.DC1

REFERENCES This article cites 56 articles, 17 of which you can access for free
http://advances.sciencemag.org/content/3/5/e1601684#BIBL

PERMISSIONS http://www.sciencemag.org/help/reprints-and-permissions

Use of this article is subject to the Terms of Service

Science Advances (ISSN 2375-2548) is published by the American Association for the Advancement of Science, 1200 New York Avenue NW, Washington, DC 20005. 2017 © The Authors, some rights reserved; exclusive licensee American Association for the Advancement of Science. No claim to original U.S. Government Works. The title *Science Advances* is a registered trademark of AAAS.

Downloaded from http://advances.sciencemag.org/ on January 18, 2018